ELECTRONIC SUPLEMENTARY MATERIAL

Dynamically Slow Solid-to-Solid Phase Transition Induced by Thermal Treatment of DimimFeCl$_4$ Magnetic Ionic Liquid

Imanol de Pedro, [a]* Oscar Fabelo, [b]* Abel García-Saiz,[a] Oriol Vallcorba, [c] Javier Junquera,[a] Jesús Angel Blanco, [d] João Carlos Waerenborgh, [e] D. Andreica, [f] Andrew Wildes, [b] María Teresa Fernández-Díaz, [b] and Jesús Rodríguez Fernández[a]

[a] CITIMAC, Facultad de Ciencias, Universidad de Cantabria, 39005 Santander.
[b] Institut Laue-Langevin, BP 156X, F-38042 Grenoble Cedex, France.
[c] ALBA Synchrotron Light Source, Cerdanyola del Vallés, Barcelona, Spain.
[d] Departamento de Física, Universidad de Oviedo, 33007 Oviedo, Spain.
[e] Centro de Ciências e Tecnologias Nucleares, Instituto Superior Técnico, Universidade de Lisboa, 2695-066 Bobadela LRS, Portugal
[f] Faculty of Physics, Babes-Bolyai University, 400084 Cluj-Napoca, Romania

Corresponding authors: depedrovm@unican.es; fabelo@ill.fr

Table of Contents

Synthesis. The synthesis of Dimim[$FeCl_4$], was performed following the method previously reported in reference 28 of the manuscript. The chemical and elemental characterization confirmed the C5N2H9Cl4Fe chemical formula. The crystal and magnetic structures were obtained by Synchrotron X-ray powder diffraction, high and low resolution neutron diffraction experiments. The physical characterization was realized using DC and AC magnetic susceptibility, magnetization, Mössbauer and muon spin relaxation measurements. Finally, density functional first-principles simulations based on a numerical atomic orbital method as implemented in the SIESTA code have been carried out.

Experimental Methods

High-resolution synchrotron X-ray diffraction (SXPD). Powder diffraction data were collected at the high resolution end station of beamline BL04 of the ALBA synchrotron using the microstrip Mythen II solid-state detector (six modules, 1280 channels/module, 50 μm/channel, sample-to-detector distance 550 mm). The wavelength used for the experiment was 0.61969 Å for all measurements except for 220 K, where a wavelength of 0.62093 Å was employed. The specimens were introduced into a 0.7 mm capillary and the temperature was controlled using an Oxford Cryostream Series 700. Sample were heated from 100 K up to 300 K and then cooled to 100 K at 5 K/min, collecting the pattern every 30 s from 2 to 45° (2θ). Longer acquisition time patterns (3 min) from 2 to 82° (2θ) were collected at 300, 220 and 100 K.

Non-polarized neutron diffraction experiments: Neutron powder diffraction measurements were performed on the D2B and D1B powder diffractometers at the Institute Laue-Langevin (ILL, Grenoble, France). About 3 g of Dimim[$FeCl_4$] were used in the experiments, this being placed in a cylindrical vanadium container and held in a liquid helium cryostat. A high-resolution powder diffractometer, D2B (λ = 1.5942 Å) was used to obtain extensive and accurate structural data at 10 and 2 K over a large angular angle $5 \leq 2\theta \leq 160^{\circ}$. High flux and medium resolution of D1B operated at λ = 2.525 Å were used to study the temperature evolution of the sample in the temperature range 2– 300 K to solve the magnetic contributions of the neutron patterns. Data from 2-10 K were collected every 0.5 K with an acquisition time of 30 min in the angular range $5 \leq 2\theta \leq 90^{\circ}$.

Polarized neutron diffraction experiments: Polarized neutron scattering experiments were carried out between 1.5 and 15 K on the diffuse scattering spectrometer D7 at the Institut Laue-Langevin (ILL). The incident wavelength and energy were 4.8 Å and the elastic Q range covered was $0.2 < Q < 2$ Å^{-1}.The total cross section was separated into magnetic, spin-incoherent, and nuclear/isotope-incoherent components using the xyz method detailed in ref 1 and 2. Data from spin-flip and non-spin-flip separations of the magnetic cross section were combined to form an average magnetic scattering cross section, $(d\sigma/d\Omega)_{mag}$. Finally, a normalization to vanadium data was performed to allow for conversion to absolute units.

Variable-temperature magnetic susceptibility measurements: Variable-temperature magnetic susceptibility measurements were performed using a standard Quantum Design MPMS magnetometer from 2 to 300 K in the $0.050 \leq H/\text{kOe} \leq 50$ range after cooling in either the presence (field cooling, FC) or the absence (zero field cooling, ZFC) of the applied field. Magnetization as a function of field (H) was measured using the same magnetometer in the $-50 \leq H/\text{kOe} \leq 50$ range at 2 and 10 K after cooling the sample in zero field. AC magnetic susceptibility measurements were carried out using the same device with an alternate excitation field (hac) of 1 Oe and frequencies from 1 to 100 Hz.

Mössbauer mesurements: Mössbauer spectra taken in the temperature range 70 K - 1.9 K were collected in transmission mode using a conventional constant-acceleration spectrometer and a

25 mCi ^{57}Co source in a Rh matrix. The velocity scale was calibrated using α-Fe foil. Low-temperature spectra were collected using a bath cryostat with the sample immersed in liquid He for measurements between 4.0 and 1.9 K, or in He exchange gas above 4.0 K (temperature stability of 0.2 K). The spectra were fitted to Lorentzian lines using a non-linear least-squares method. Isomer shifts (Table S6) are given relative to metallic α-Fe at room temperature.

Muon spin relaxation (μSR) spectroscopy: Muon spin relaxation (μSR) experiments were performed in zero applied field at the Laboratory for Muon Spin Spectroscopy of the Paul Scherrer Institute, Switzerland using the GPS spectrometer in the temperature range 1.6–220 K. The sample was grinded and mounted in a special "cup shape" aluminum container covered with a thin layer of mylar tape to prevent leakage. Before cooling to the lowest temperature, a calibration run was recorded, in weak transverse field, at 10 K. The calibration run at 10 K offers information about the amplitude of the μSR signal and about a geometrical factor of the experiment. It is also recommended in order to ensure that of all the parts of the system are cooled down and secures a low and stable base temperature.

DFT calculations. Computational details: We have carried out density functional first-principles simulations on phase **I-a** and **I-b** based on a numerical atomic orbital method as implemented in the SIESTA[3] code. All the calculations have been performed within the efficient implementation[4] of the vdw density functional of Dion et al.[5] This fully non-local vdw correlation has been recently tested on imidazolium-based ionic liquids [6], showing spectacular improvements in the interatomic geometries, equilibrium volume and internal geometry with respect to the local density (LDA) and generalized gradient approximation (GGA) at a very modest computational cost.

Core electrons were replaced by ab-initio norm conserving pseudopotentials, generated using the Troullier-Martins scheme [7], in the Kleinman-Bylander fully non-local separable representation [8]. In order to avoid the spiky oscillations close to the nucleus we have included small partial core corrections [9] for all the atoms. The reference configuration and cutoff radii for each angular momentum shell and the matching radius between the full core charge density and the partial core charge density for the nonlinear core corrections (NLCCs) for the pseudopotentials used in this work can be found in Table S.1 of Supporting Information for H, C, N, Br and Fe.

The one-electron Kohn-Sham eigenstates were expanded on a basis of strictly localized numerical atomic orbitals [10]. We used a double-ζ plus polarization for the valence states of all the atoms. The atomic shells explicitly included in the simulations are the 1s, 2p for H; 2s, 2p, 3d for C and N; 4s, 4p, 4d for Br; and 4s, 4p, 3d for Fe. All the parameters that define the shape and range of the basis functions were obtained by a variational optimization of the enthalpy [11] (with a pressure P=0.1 GPa), using the coordinates of Dimim[$FeBr_4$] obtained by Rietveld refinement from high resolution neutron powder diffraction data as the reference configuration.

The electronic density, Hartree, and exchange correlation potentials, as well as the corresponding matrix elements between the basis orbitals, were calculated in a uniform real space grid. An equivalent plane wave cut-off of 350 Ry was used to represent the charge density. For the Brillouin zone integrations we use a Monkhorst-Pack sampling [12] of 4 × 2 × 4, equivalent to a real-space cut-off of 10 Å. [13]

Starting from the experimental coordinates obtained by high resolution neutron powder diffraction data at 10 K, a full optimization of the crystal lattice parameters and atomic positions was carried out, until a maximum component of the force on any atom was smaller than 0.01 eV/Å and the maximum component of the stress tensor was smaller than 0.0001 eV/Å^3.

The intramolecular geometries and distances of the $[Dimim]^+$ cation and $[FeCl_4]^-$ anion obtained by DFT calculations lie in the expected range comparable to those found in experimental data (overestimation within the range from 2 to 3 %). The intermolecular distances and orientations are in good agreement with the experimental results, thus confirming that the vdw functional does not introduce any unwanted features in the description of the low temperature structure. [4]

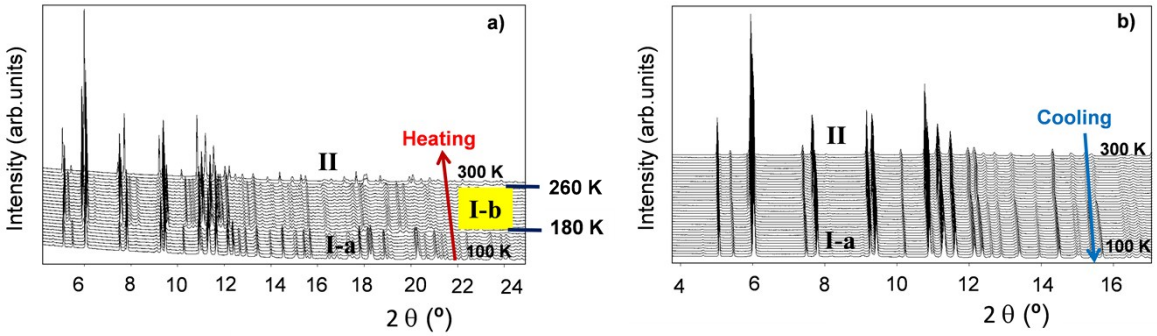

Figure S1. SXRD thermodiffractogram of Dimim$[FeCl]_4$ heating from 100 to 300 K after a thermal quenching using a cryo-stream device and cooling between 300 and 100 K at 5 K /min

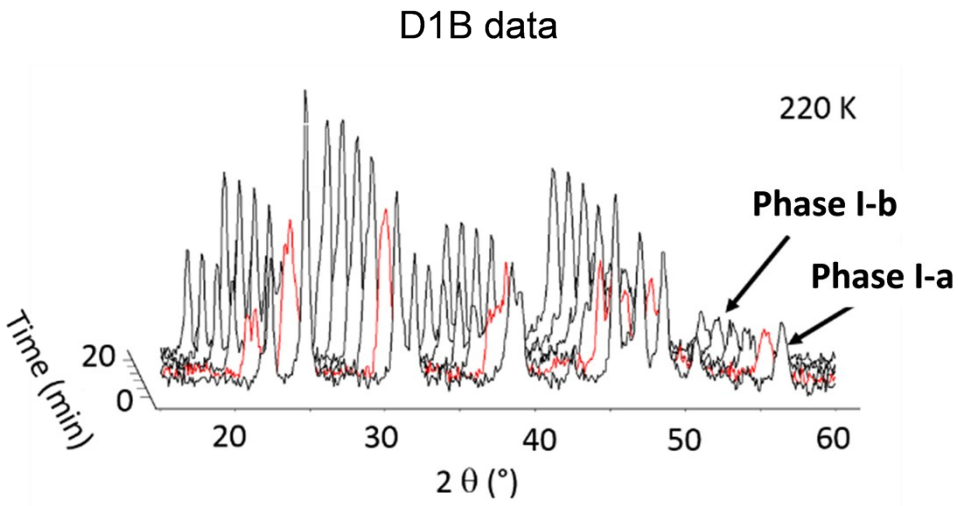

Figure S2. Neutron diffractograms collected at D1B diffractometer at 220 K in function of time. The red line show the spectra where the phase **I-a** starts to transit to phase **I-b.**

Powder data solution and refinement. In order to determine the crystal structure of phase **I-b**, we use in a first step low temperature synchrotron powder data (ca. 220 K). The diffraction patterns collected at BL04-MSPD beamline at ALBA synchrotron (Barcelona, Spain), were indexed using DICVOL04 [14] and a whole-pattern matching and intensity extraction were performed with DAjust software.[15] The intensities were introduced in the direct-space solution program TALP[16] to obtain the candidate solution that was finally refined with the restrained Rietveld refinement program RIBOLS[17] using distance restraints taken from MOGUL.[18] For SXPD refinements, H atoms were placed in calculated positions and constrained to the respective C atoms. The Rietveld analysis was completed using a multipattern approach, combining the synchrotron data with the high resolution neutron diffraction pattern. The quality of the data allow to refine the hydrogen atoms during the last Rietveld refinement, using as starting point the hydrogen atoms coordinates of derived from Density Functional Theory (DFT) calculations.

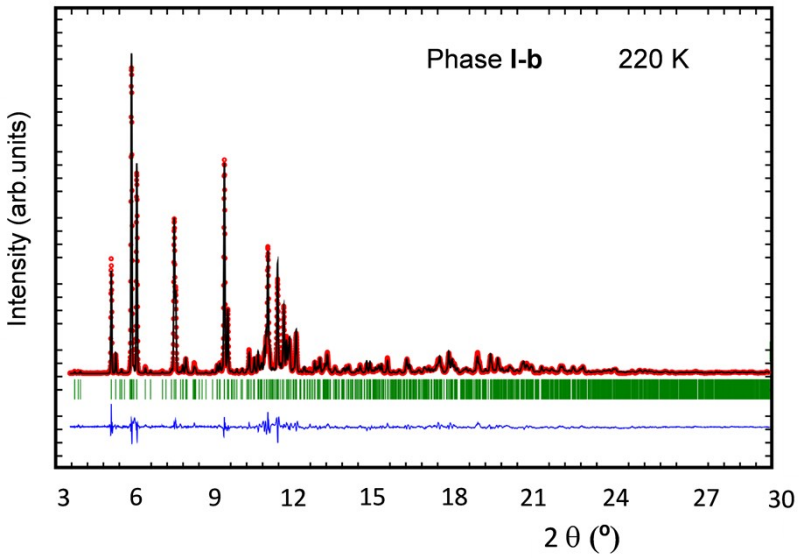

Figure S3. Observed (red points) and calculated (black solid line) SXPD patterns for phase **I-b** at 220 K. Positions of the Bragg reflections are represented by vertical bars. The observed-calculated difference patterns are depicted at the bottom of the figure.

Magnetometry measurements. The magnetic field dependence of the maxima of both phases with the applied magnetic field was studied with another set of DC magnetic susceptibility measurements from 1 to 50 kOe, between 2 and 15 K after cooling in absence of the applied field (see Figure S4). On one hand, χ_m maxima of phase **I-a** located near of 3.1 K under 1 kOe field does not change when the magnetic field increases up to 10 kOe, disappearing for fields higher than 20 kOe. This suggests a partial overcome of the antiferromagnetic interactions present in the phase **I-a**. On the other hand, the behaviour of χ_m as a function of the external magnetic field in the phase **I-b** is slightly different, the maximum of χ_m is shifted to lower temperatures, being located at 4.15 K for an applied field of 50 kOe, suggesting that the antiferromagnetic interactions remain mainly unchanged.

The possible dynamical response of the magnetic ordering of both phases up to 2 K was checked by AC magnetic susceptibility measurements with an alternate excitation field (H_{ac}) of amplitude 1 Oe and frequencies from 1 to 100 Hz (Figure S5). The curves confirm the existence of long range order interactions and exclude the existence of a possible dynamical magnetic process up to 2 K (no-dependence of the position of magnetic peak on the frequency).[19, 20] The weak absorption in the imaginary component, χ'', in this temperature range ratifies the presence of an antiferromagnetic order, in good agreement with the results obtained above from the static magnetic susceptibility data.

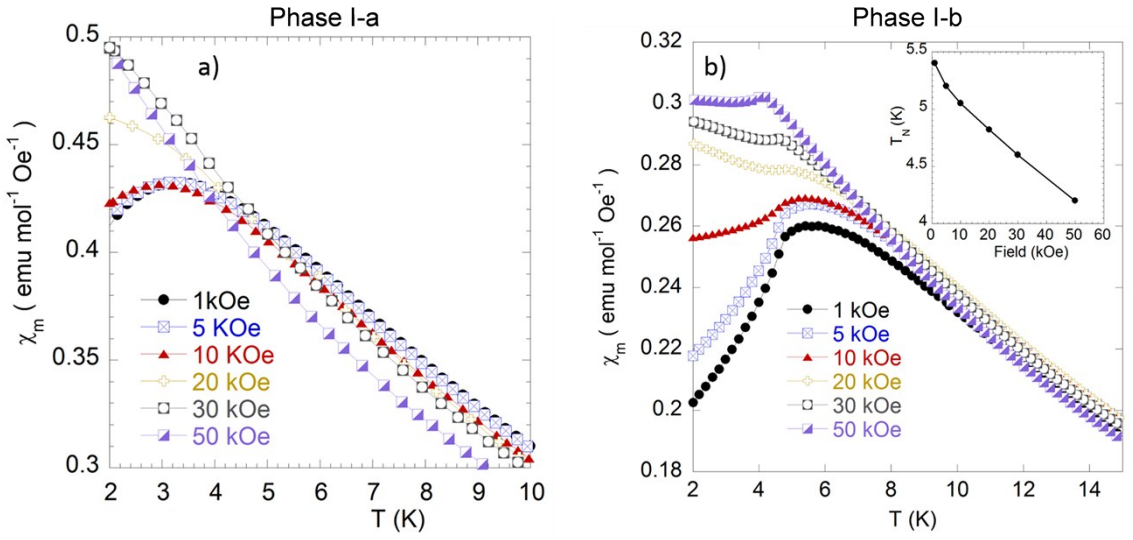

Figure S4. Low temperature ZFC magnetic susceptibility for phase **I-a** and **I-b** at different fields from 1 to 50 kOe. The inset o figure b shows the evolution of Néel temperature (T_N) with the applied magnetic field.

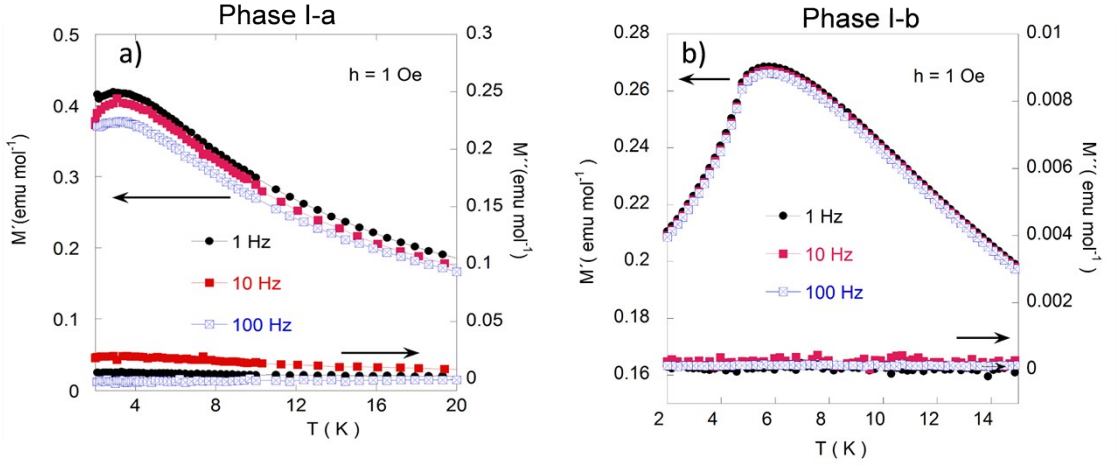

Figure S5. Temperature dependence of the real (χ') and imaginary (χ'') components of the ac magnetic susceptibility for phase **I-a** and **I-b** measured under an ac field hac = 1 Oe and frequencies from 1 to 100 Hz.

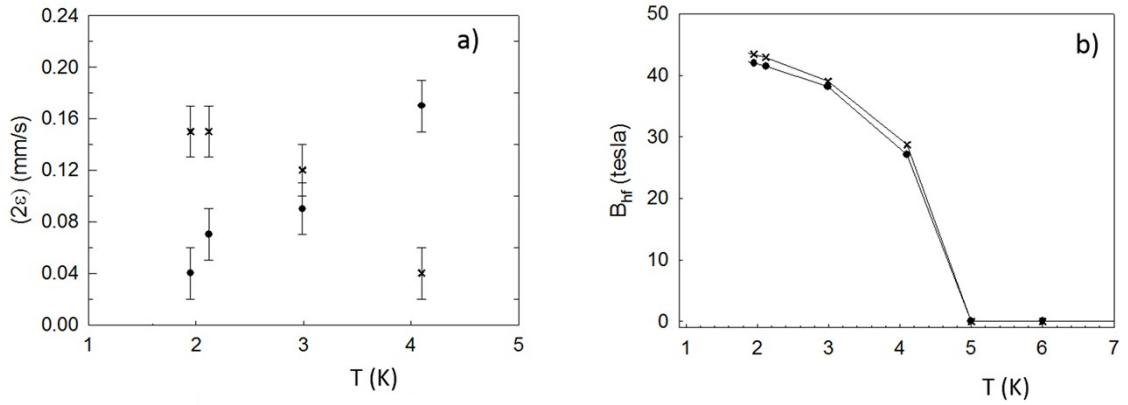

Figure S6. (a) Temperature dependence of (2ε) and (b) B_{hf} for both magnetic sublattices of phase **I-b**.

Both magnetic sextets have equal area within experimental error (Table S6), in agreement with two different Fe^{3+} magnetic sublattices. Quadrupole shifts, (2ε), are also different for each sextet which is related with occurrence of two different directions of iron magnetic moments with respect to the crystallographic axes. The temperature dependence of the (2ε) values (Table S6 Figure S6) of phase **I-b** suggest that the magnetic moment directions gradually change with temperature between T_N and 1.9 K.

Muon Spin Spectroscopy details and refinements

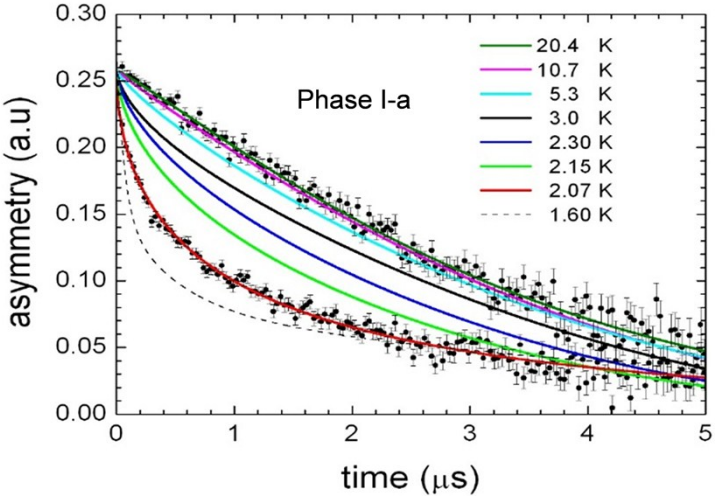

Figure S7. Examples of μSR spectra of phase **I-a** recorded at low temperatures. Lines are fits of the data using the fit function specified in the text: $KT \cdot e^{-(\lambda t)^{\beta}}$.

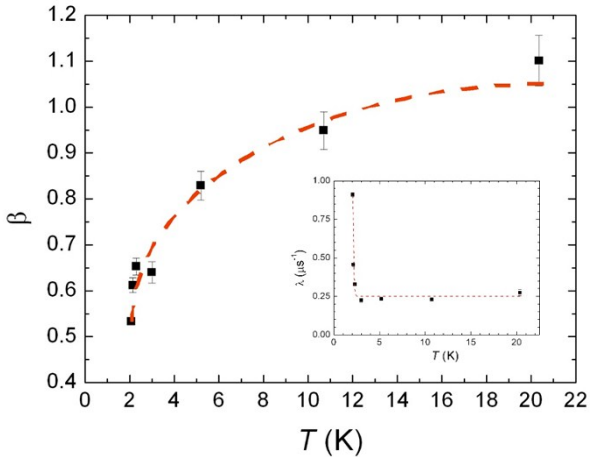

Figure S8. Temperature dependence of the fit parameter β and λ (inset) of phase **I-a**. The line is guide to the eye. β gradually decreases down to about 0.5 at 2.07 K , while λ drastically increases from 0.25 at 5 K to 0.90 at 2.07 K.

Data below 2.07 K spectra were fitted using a combination of fast (2/3 term) /slow (1/3 term) relaxing exponentials with an amplitude ratio of about 2/1, as expected for a magnetic sample: $AP(t) = \left(A_1 e^{-\lambda_1 t} + A_2 e^{-\lambda_2 t}\right) + A_3 e^{-\lambda_3 t}$. Recall that in the magnetic phase of a sample the muons ensemble is, in general, fast depolarized. An average of 2/3 of the muons (2 parts) will see magnetic fields perpendicular to their initial polarization ⇨ they perform Larmor precession around those fields, while 1/3 of the muons (one part) will sense magnetic fields parallel to their initial polarization and therefore will not process. Those muons are even not depolarized if the magnetism of the sample is static (neither a field distribution parallel to the initial polarization nor field dynamics along the initial muon polarization will produce depolarization/relaxation of the muon spin). However, if field fluctuations perpendicular to the muon spin are present, they can

induce spin-flips and the 1/3 term becomes time dependent (exponential). The amplitude ratio of the 1/3 term (relaxing) and the 2/3 term (oscillating or fast depolarized) is 1/2. The "magnetic part" of the μSR spectra of phase **I-a** could be described by a purely exponential $A_{magn}P_{magn}(t)$, i.e. no oscillations are observed in the μ_{SR} spectra. The fitted spectra are displayed in Figure S9 and the temperature dependence of the fast relaxation rates λ_1 and λ_2 in Figure S10. These μ_{SR} data, confirms the onset of a magnetic ordering detected by magnetization and Mössbauer measurements in phase **I-a** at low temperatures. In addition, the values of λ_3 are similar to those of λ at high temperatures, indicating that the ordering below 2 K could be not static.

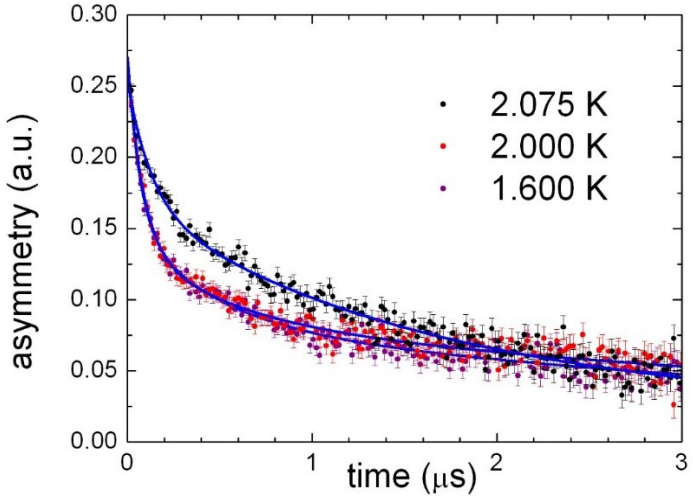

Figure S9. μSR spectra of phase **I-a** fitted using a combination of exponentials, as described in the text.

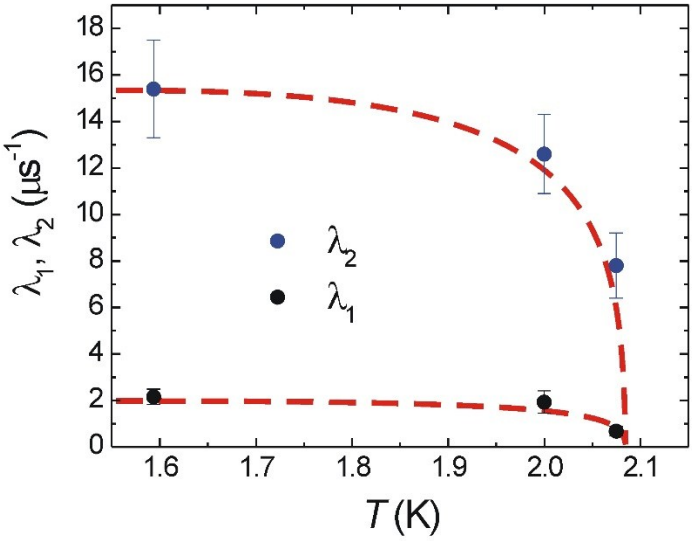

Figure S10. Temperature dependence of λ_1 and λ_2 of phase **I-a**. The lines are guide to the eye.

The μSR spectra recorded 5.23 K of phase **I-b** (one can observe that a fast component develops below this temperature) indicates that the sample becomes magnetic. These data could be fitted using 4 oscillatory components (Figure S11),

$$AP(t) = A_1 e^{-\lambda_1 t}\cos(2\pi\nu_1 t + \varphi_1) + A_2 e^{-\lambda_2 t}\cos(2\pi\nu_2 t + \varphi_2) + \\ + A_3 e^{-\lambda_3 t}\cos(2\pi\nu_3 t + \varphi_3) + A_4 e^{-\lambda_4 t}\cos(2\pi\nu_4 t + \varphi_4) + A_5 e^{-\lambda_5 t} + A_6 e^{-\lambda_6 t} \quad (3)$$

The four oscillatory terms describe the behavior of muons stopped in an interstitial site where they "see" magnetic field: $\nu_i = \frac{\gamma}{2\pi} B_i$. Not all the phases in eq. 3 are close to zero, which can be understood as a wide field distribution. The fifth term, corresponds to muons sensing a large local field and/or field distribution, so large that the signal disappears before the first half of an oscillation. The last term is the 1/3 term, see the discussion above. The following equalities hold: $\frac{\sum_1^6 A_i}{3} = A_6$ or $\frac{\sum_1^5 A_i}{2} = A_6$ i.e. the sum of the amplitudes of the μSR signals corresponding to the fast depolarized signals is twice the amplitude of the μSR signal corresponding to the non-oscillating small relaxing term.

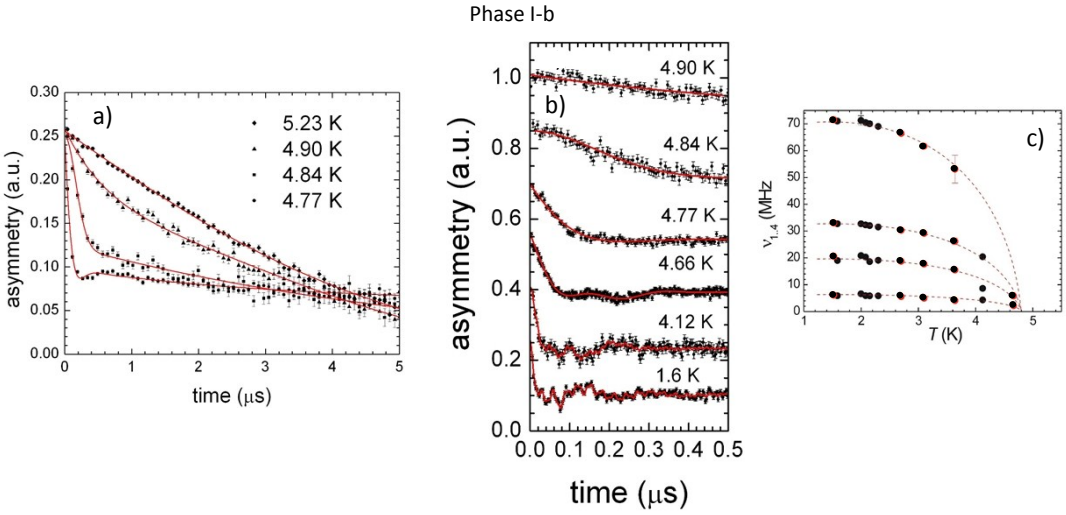

Figure S11.a) Magnetic transition is in-between 4.9 and 5.23 K of phase **I-b**. b) μSR spectra recorded below 4.90 K. c) The temperature dependence of the fitted frequencies.

Detail of magnetic structure determination The possible magnetic structures, were checked using Bertaut's symmetry analysis method.[21] The irreducible representations (irreps) compatible with the indexed propagation vector [**k** = (0, 0, 0)] allows us to determine the symmetry constraints between the different magnetic moments of the Fe^{3+} atom within the magnetic unit cell. The total magnetic representation of the propagation vector group can be decomposed on four irreducible representations, all of them one-dimensional. The Γ_{mag} can be represented as Eq (4):

$$\Gamma_{mag} = 3(\Gamma_1 \oplus \Gamma_2 \oplus \Gamma_3 \oplus \Gamma_4). \qquad (4)$$

The magnetic moment of the $Fe(1)^{3+}$ and $Fe(2)^{3+}$ sites, both located on the 4*e* Wyckoff positions, are obtained from the basis vectors as; $\mathbf{m}_{4e}(1)$ = (u, v, w), $\mathbf{m}_{4e}(2)$ = (-u, v, -w), $\mathbf{m}_{4e}(3)$ = (-u, -v, -w) and $\mathbf{m}_{4e}(4)$ = (u, -v, w) for *irrep* Γ_1. For $\mathbf{m}_{4e}(1)$ = (u, v, w), $\mathbf{m}_{4e}(2)$ = (-u, v, -w), $\mathbf{m}_{4e}(3)$ = (u, v, w) and $\mathbf{m}_{4e}(4)$ = (-u, v, -w), the Γ_3 presents $\mathbf{m}_{4e}(1)$ = (u, v, w), $\mathbf{m}_{4e}(2)$ = (u, -v, w), $\mathbf{m}_{4e}(3)$ = (-u, -v, -w) and $\mathbf{m}_{4e}(4)$ = (-u, v, -w) while Γ_4 give rise to $\mathbf{m}_{4e}(1)$ = (u, v, w), $\mathbf{m}_{4e}(2)$ = (u, -v, w), $\mathbf{m}_{4e}(3)$ = (u, v, w) and $\mathbf{m}_{4e}(4)$ = (u, -v, w). In all cases there are three degrees of freedom (u, v, w) for each $Fe(1)^{3+}$ and $Fe(2)^{3+}$ sites, and therefore the global degree of freedom is six (see Table S7).

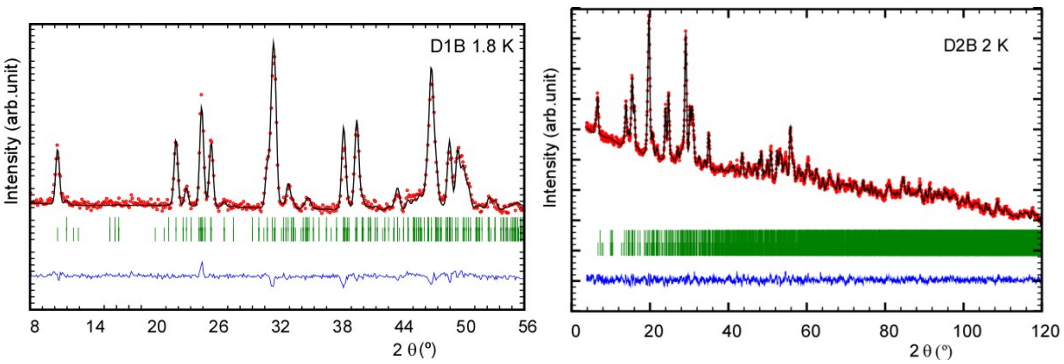

Figure S12. D1B and D2B neutron diffraction data of phase **I-a** at 1.8 and 2 K, respectively. Positions of the Bragg reflections for the nuclear (first row) and magnetic (second row) structures are presented. The difference curves are plotted at the bottom.

Rietveld refinement of the D1B (1.8 K) and D2B (2 K) patterns, where the atomic coordinates and isotropic temperature factors of the nuclear part were fixed to those obtained from the D2B pattern at 10 K, shows that Γ_1 is the only irrep that provides a satisfactory agreement between the calculated and the experimental diffraction pattern.

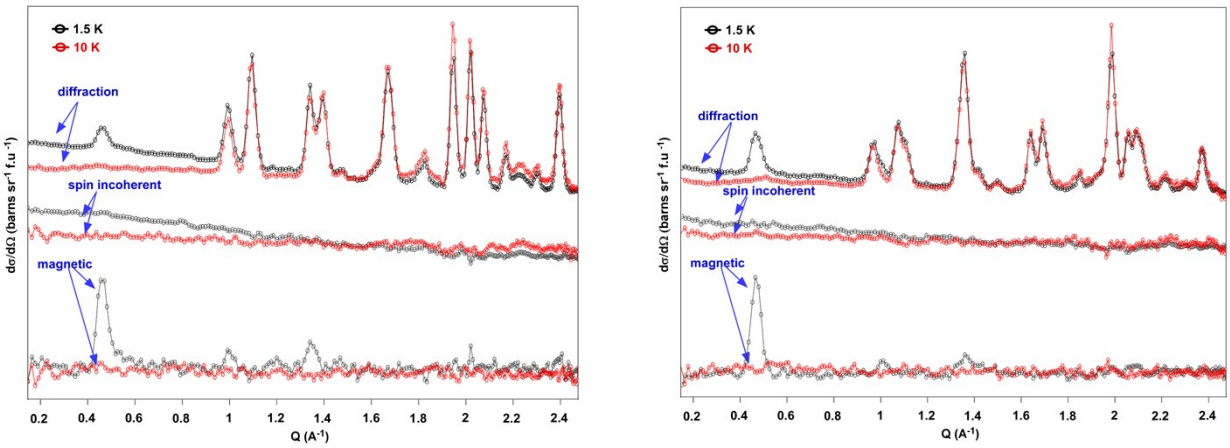

Figure S13. Separation of neutron scattering cross sections, nuclear and spin incoherent magnetic from a powdered sample of phases **I-a** (left) and **I-b** (right) of Dimim[$FeCl_4$] at 1.5 (3D magnetic ordered state) and 10 K (paramagnetic state) measured using xyz-polarization analysis on D7.

DFT calculations of anion-π interactions. Taking the intermolecular distances obtained by high resolution NPD at 10 K and comparing them with IUPAC recommendation[22] [bonding contact should be shorter than the sum of the vdw (≤ 3.65 Å)], only phase **I-b** displays notable features that would support the existence of attractive anion-π interactions[23] [where chloride should be located over the center of the π system (θ = 90 ± 10º)]. To further check their presence in the condensed phase at 0 K, we obtain the projected density of states (PDOS) of the imidazolium with the chloride of the metal complex anion, [Figure S13]. We detected an extensive range of energies between 0 and -3 eV below the Fermi energy, where the PDOS reach a non-zero value, evidencing the existence of a bonding between them. To visualize the shape of one of these states, we have selected a representative state at the Gamma point, with an energy of -2.34 eV below the Fermi energy [Figure S13]. The isosurface for a value of the wave function of 0.012 displays how the wave function can connect Fe(1) and Fe(2) from layer to layer across the π orbital of the imidazolium ring (see Figure 10 of the article).

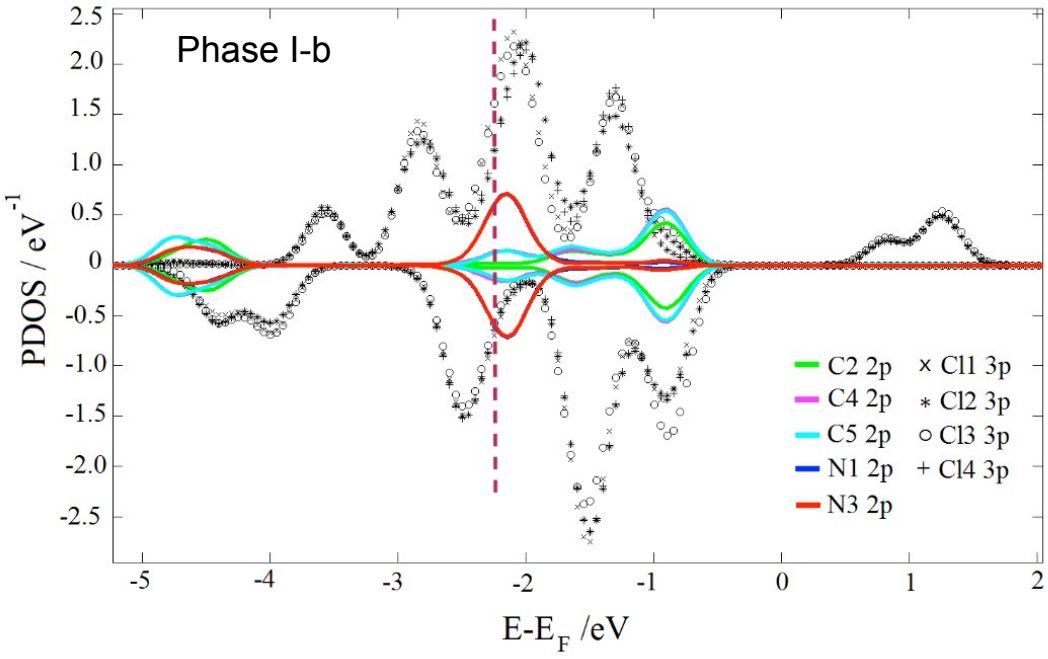

Figure S14: PDOS of clhorides from a $[FeCl_4]^-$ ion (black marks) with the atoms in the imidazolium ring (color lines). Dashed line shows the state with energy of −2.34 eV below the Fermi energy, where there is orbital overlapping.

Table S1. Crystallographic data and structure refinement details for $DiminFeCl_4$ from SXPD data at 300 K (phase **II**), 100 K (phase **I-a**) and 220 K (phase **I-b**).

	$DiminFeCl_4$ at 300K	**$DiminFeCl_4$ at 100K**	**$DiminFeCl_4$ at 220K**
Molecular formula	$C_5H_9N_2$, Cl_4Fe	$C_5H_9N_2$, Cl_4Fe	$C_5H_9N_2$, Cl_4Fe
Formula weight	294.79	294.79	294.79
Crystal System	monoclinic	orthorhombic	monoclinic
Space group	$P2_1$	$P2_12_12_1$	$P2_1/c$
a (Å)	6.5434(2)	9.1242(1)	14.1391(3)
b (Å)	14.0286(2)	13.8132(2)	13.7039(3)
c (Å)	6.5314(2)	9.0359(1)	13.2935(3)
α (º)	90.0	90.0	90.0
β (º)	89.921(1)	90.0	115.539(2)
γ (º)		90.0	90.0
Volume (Å^3)	599.55(4)	1138.84(2)	2324(4)
Z	2	4	8
Calculated density (g/cm^3)	1.633	1.719	1.685
Measurement temp. (K)	300	100	220
Wavelength (Å)	0.61969	0.61969	0.62093
Measured 2θ range, step (º)	1.104 to 63.096, 0.006	1.104 to 63.096, 0.006	1.998 to 30.171, 0.004
Rietveld refinement details:			
Profile function	Pseudo-Voigt	Pseudo-Voigt	Pseudo-Voigt
2θ range used (º)	4.006 to 40.000	3.006 to 40.002	3.604 to 30.171
Num. of reflections	888	948	1442
Data points	5999	6166	6643
Parameters[a]	50[b]	50[a]	87[b]
Restraints	33	16	46
R_{wp}	0.061	0.058	0.037
R_{exp}	0.010	0.010	0.005
$\chi_{Rietveld}/\chi_{Pattern\text{-}Matching}$	1.421	1.241	2.295

[a]*Parameters: Atomic coordinates (x,y,z), isotropic atomic displacement parameters (dimim, Cl, Fe), 6 profile parameters, zero offset, scale factor, cell parameters.*
[b] *Restraints: Bond distances, angles and dimim plane.*

Table S2. Crystallographic data and structure refinement details for $DiminFeCl_4$ from high resolution NPD data at 10 K for phase **I-a** and phase **I-b**.

	Phase Ia	**Phase Ib**
Molecular formula	$C_5H_9N_2$, Cl_4Fe	$C_5H_9N_2$, Cl_4Fe
Formula weight	294.79	294.79
Crystal System	Orthorhombic	Monoclinic
Space group	$P2_12_12_1$	$P2_1/c$
a (Å)	9.0897(2)	13.9037(6)
b (Å)	13.7423(3)	13.5621(6)
c (Å)	8.97670(19)	13.1303(6)
α (º)	90.0	90.0
β (º)	90.0	115.453(3)
γ (º)	90.0	90.0
Volume (Å^3)	1121.31(4)	2235.59(16)
Z	4	8
Calculated density (g/cm^3)	1.746	1.752
Measurement Temperature (K)	10K	10K
Radiation (wavelengths in Å)	1.5942	1.5942
Measured 2θ range, stepsize (º)	0.00–159.95, 0.05	0.00–159.95, 0.05
Rietveld refinement details:		
Profile function	Pseudo-Voigt	Pseudo-Voigt
2θ range used (º)	6.00 to 140.0	6.00 to 120.00
Num. of reflections	1336	4529
Data points	2680	2280
Parameters	77	141
Restraints	43	86
R_{wp}	0.012	0.011
R_{exp}	0.009	0.010
$\chi_{Rietveld}/\chi_{Pattern\text{-}Matching}$	1.512	1.613

Table S3. Final refined positional coordinates from SXPD and high resolution NPD pattern of Dimim[$FeCl_4$] at 300 K (phase **II**). Label of the atoms as in Figure 10.

	Dimim[$FeCl_4$] at 300K[a] from SXPD			Dimim[$FeCl_4$] at 300K[b][28] from NPD		
Atom	*x/a*	*y/b*	*z/c*	*x/a*	*y/b*	*z/c*
Fe	0.2366(7)	0.35963(7)	0.2652(4)	0.2240(24)	0.3624(23)	0.2581(24)
Cl1	0.1158(18)	0.2334(9)	0.4198(4)	0.0774(47)	0.2310(27)	0.3821(51)
Cl2	0.1951(11)	0.3617(12)	-0.0539(4)	0.1397(46)	0.3776(31)	-0.0635(28)
Cl3	0.1309(19)	0.4905(8)	0.4140(4)	0.0889(55)	0.4864(29)	0.4112(50)
Cl4	0.5722(7)	0.3522(11)	0.3336(4)	0.5520(25)	0.3620(29)	0.2987(36)
N1	0.384(3)	0.6492(9)	0.0546(4)	0.4209(32)	0.6507(15)	0.0900(35)
C2	0.426(3)	0.5927(10)	-0.1017(4)	0.3990(31)	0.6055(16)	-0.0836(35)
N3	0.615(3)	0.5580(9)	-0.0759(4)	0.5629(34)	0.5551(15)	-0.1278(34)
C4	0.690(3)	0.5930(11)	0.1014(4)	0.6911(31)	0.5672(16)	0.0243(36)
C5	0.551(3)	0.6507(11)	0.1759(4)	0.6025(33)	0.6259(16)	0.1617(34)
C1'	0.193(3)	0.7033(10)	0.0759(4)	0.2770(38)	0.7108(16)	0.1800(42)
C1"	0.717(4)	0.4870(8)	-0.2048(4)	0.5768(44)	0.4978(16)	-0.3023(35)
H2	0.33480	0.58170	-0.20830	0.2699(35)	0.6096(19)	-0.1794(43)
H4	0.81550	0.57570	0.15690	0.8345(33)	0.5344(16)	0.0413(46)
H5	0.57210	0.68530	0.29550	0.6734(42)	0.6487(18)	0.2964(34)
H1A'	0.21730	0.77070	0.06960	0.1307(37)	0.6884(42)	0.1302(98)
H1B'	0.10710	0.68480	-0.03660	0.3039(91)	0.7824(16)	0.1314(99)
H1C'	0.12520	0.68820	0.20250	0.2825(93)	0.7016(46)	0.3422(42)
H1A"	0.72050	0.50980	-0.34330	0.4324(71)	0.4987(35)	-0.3794(50)
H1B"	0.85290	0.47280	-0.15990	0.6895(57)	0.5215(36)	-0.4058(67)
H1C"	0.63470	0.43020	-0.19820	0.5936(98)	0.4241(16)	-0.2621(52)

Full occupancies for all atoms.
(a) a = 6.5434(2) Å, b = 14.0286(2) Å, c = 6.5314(2) Å, $\alpha = \gamma = 90º$, β = 89.921(1)º, s.g. $P2_1$. B_{Fe} = 7.4(1) Å^2; B_{Cl} = 8.1(1) Å^2; $B_{C,H}$ = 10.2(1) Å^2.
(b) a = 6.5419(27) Å, b = 14.0374(26) Å, c = 6.5357(30) Å, $\alpha = \gamma = 90º$, β = 90.006(23) º, s.g. $P2_1$. $B_{overall}$ = 5.4(9) Å^2 ..

Table S4. Final refined positional coordinates from SXPD at 100 K and high resolution NPD pattern at 10 K of Dimim[$FeCl_4$] (phase **I-a**). Label of the atoms as in Figure 10.

	Dimim[$FeCl_4$] at 100K[a]			Dimim[$FeCl_4$] at 10K[b]		
Atom	*x/a*	*y/b*	*z/c*	*x/a*	*y/b*	*z/c*
Fe	0.2564(2)	0.2478(4)	0.2610(4)	0.2582(6)	0.2462(7)	0.2683(8)
Cl1	0.3986(5)	0.3757(3)	0.2302(4)	0.4019(8)	0.3728(5)	0.2267(9)
Cl2	0.1079(4)	0.2362(5)	0.0727(4)	0.1031(8)	0.2359(5)	0.0764(6)
Cl3	0.3818(5)	0.1106(3)	0.2810(4)	0.3799(9)	0.1055(5)	0.2870(8)
Cl4	0.1305(4)	0.2729(4)	0.4643(4)	0.1329(9)	0.2734(6)	0.4730(7)
N1	-0.0757(13)	0.4519(11)	0.2411(4)	-0.0700(6)	0.4539(4)	0.2437(4)
C2	0.0113(17)	0.4947(15)	0.3407(4)	0.0187(8)	0.4947(6)	0.3421(3)
N3	0.1042(13)	0.5513(10)	0.2651(4)	0.1119(6)	0.5526(4)	0.2645(4)
C4	0.0742(13)	0.5441(10)	0.1155(4)	0.0829(9)	0.5475(7)	0.1210(4)
C5	-0.0402(15)	0.4838(11)	0.1009(4)	-0.0292(9)	0.4825(6)	0.1070(3)
C1'	-0.1913(12)	0.3825(10)	0.2860(4)	-0.18449(14)	0.38529(9)	0.28813(10)
C1"	0.2228(13)	0.6094(11)	0.3319(4)	0.22694(15)	0.61194(8)	0.33338(12)
H2	0.00240	0.48860	0.45760	0.032(4)	0.482(3)	0.4550(7)
H4	0.13570	0.58080	0.03590	0.139(3)	0.587(2)	0.042(2)
H5	-0.08870	0.45740	0.00410	-0.074(3)	0.454(2)	0.0101(17)
H1A'	-0.29030	0.39100	0.22580	-0.137(3)	0.3217(11)	0.326(3)
H1B'	-0.14360	0.31530	0.26430	-0.262(2)	0.413(2)	0.360(2)
H1C'	-0.20970	0.39120	0.40130	0.3270(15)	0.5839(20)	0.300(3)
H1A"	0.30660	0.56260	0.36590	0.224(3)	0.6821(9)	0.293(3)
H1B"	0.26220	0.65730	0.24910	0.209(3)	0.614(2)	0.4469(6)
H1C"	0.17970	0.64840	0.42270	0.2582(6)	0.2462(7)	0.2683(8)

Full occupancies for all atoms.
(a) $a = a = 9.1242(1)$ Å, $b = 13.8132(2)$ Å, $c = 9.0359(1)$ Å, $\alpha = \beta = \gamma = 90^o$, s.g. $P2_12_12_1$. $B_{Fe} = 2.3(1)$ Å^2; $B_{Cl} = 2.9(1)$ Å^2; $B_{C,H} = 2.5(1)$ Å^2.
(b) $a = 9.0897(2)$ Å, $b = 13.7423(3)$ Å, $c = 9.9767(19)$ Å, $\alpha = \beta = \gamma = 90^o$, s.g. $P2_12_12_1$. $B_{overall} = B_{Fe} = 0.3(1)$ Å^2; $B_{Cl} = 0.4(1)$ Å^2; $B_N = 0.6(1)$ Å^2, $B_C = 0.3(1)$ Å^2, $B_H = 4.0(2)$ Å^2.

Table S5. Final refined positional coordinates from SXPD at 220 K and high resolution NPD at 10 K of Dimim[$FeCl_4$] (phase **I-b**). Label of the atoms as in Figure 10.

	Dimim[$FeCl_4$] at 220K[a]			Dimim[$FeCl_4$] at 10K[b]		
Atom	*x/a*	*y/b*	*z/c*	*x/a*	*y/b*	*z/c*
Fe1	0.4018(4)	0.2525(6)	0.0628(4)	0.4059(13)	0.2547(13)	0.0660(13)
Cl1	0.4494(8)	0.1094(8)	0.0216(4)	0.4432(14)	0.1065(11)	0.0160(13)
Cl2	0.4331(7)	0.2594(9)	0.2376(4)	0.4302(13)	0.2617(13)	0.2397(15)
Cl3	0.4890(7)	0.3649(8)	0.0248(4)	0.4867(14)	0.3682(12)	0.0212(16)
Cl4	0.2389(8)	0.2708(8)	-0.0331(4)	0.2313(13)	0.2789(13)	-0.0373(14)
N1	0.2514(19)	0.5235(11)	0.0499(4)	0.2590(7)	0.5295(13)	0.0429(3)
C2	0.1870(17)	0.4728(11)	0.0797(4)	0.1982(9)	0.4822(17)	0.0793(4)
N3	0.2344(18)	0.4534(10)	0.1861(4)	0.2455(7)	0.4666(12)	0.1910(5)
C4	0.3305(18)	0.4904(12)	0.2244(4)	0.3386(10)	0.5097(16)	0.2294(2)
C5	0.3401(17)	0.5341(11)	0.1394(4)	0.3435(7)	0.5508(15)	0.1376(4)
C1'	0.228(2)	0.5591(12)	-0.0615(4)	0.22921(14)	0.55319(13)	-0.0752(2)
C1''	0.1915(19)	0.3991(11)	0.2527(4)	0.20866(16)	0.40398(16)	0.25791(17)
H2	0.119	0.4537	0.0328	0.124(2)	0.458(4)	0.023(4)
H4	0.3823	0.4872	0.2973	0.389(4)	0.514(5)	0.3145(12)
H5	0.3988	0.5671	0.1426	0.408(3)	0.585(4)	0.133(5)
H1A'	0.2947	0.5664	-0.0635	0.299(2)	0.537(4)	-0.081(5)
H1B'	0.1881	0.5094	-0.1133	0.168(3)	0.509(4)	-0.129(4)
H1C'	0.1905	0.6198	-0.0815	0.212(5)	0.6270(12)	-0.093(5)
H1B''	0.1315	0.3572	0.2182	0.222(5)	0.442(4)	0.331(3)
H1A''	0.1787	0.4457	0.2993	0.1281(9)	0.398(4)	0.207(4)
H1C''	0.2518	0.3605	0.2972	0.248(4)	0.338(2)	0.284(5)
Fe2	0.0841(5)	0.7404(5)	0.1486(4)	0.0933(13)	0.7399(14)	0.1480(13)
Cl1b	0.0274(9)	0.6192(8)	0.2207(4)	0.0251(14)	0.6172(13)	0.2141(14)
Cl2b	0.2558(7)	0.7472(10)	0.2413(4)	0.2609(11)	0.7454(14)	0.2433(13)
Cl3b	0.0210(8)	0.8856(7)	0.1611(4)	0.0184(13)	0.8833(13)	0.1566(14)
Cl4b	0.0395(7)	0.7106(6)	-0.0290(4)	0.0540(13)	0.7048(12)	-0.0253(14)
N1b	0.2925(13)	0.9244(11)	0.0779(4)	0.2870(7)	0.9306(9)	0.0785(7)
C2b	0.2142(13)	0.9835(12)	0.0574(4)	0.2057(8)	0.9936(11)	0.0570(8)
N3b	0.2299(16)	1.0375(11)	0.1457(4)	0.2293(6)	1.0525(9)	0.1434(7)
C4b	0.3246(17)	1.0106(14)	0.2266(4)	0.3255(5)	1.0260(7)	0.2204(9)
C5b	0.3637(14)	0.9403(13)	0.1866(4)	0.3610(9)	0.9479(12)	0.1808(9)
C1'b	0.3100(17)	0.8495(12)	0.0084(4)	0.29487(13)	0.85235(17)	0.00514(19)
C1''b	0.1616(18)	1.1173(12)	0.1594(4)	0.16357(16)	1.12610(18)	0.16487(15)
H2b	0.1573	0.9864	-0.017	0.134(2)	1.001(4)	-0.014(3)
H4b	0.3574	1.0315	0.2985	0.431(2)	0.908(4)	0.220(5)
H5b	0.425	0.9078	0.2155	0.375(4)	1.072(3)	0.285(3)
H1A''b	0.2038	1.1604	0.2189	0.166(5)	1.125(5)	0.244(2)
H1B''b	0.1288	1.1538	0.0913	0.182(5)	1.191(2)	0.136(4)
H1C''b	0.1087	1.0879	0.1766	0.0837(11)	1.120(5)	0.111(4)
H1A'b	0.3783	0.8597	0.0116	0.359(3)	0.866(5)	-0.012(4)
H1B'b	0.3097	0.7904	0.047	0.308(5)	0.7850(20)	0.045(4)
H1C'b	0.2594	0.8445	-0.068	0.223(3)	0.847(5)	-0.066(3)

Full occupancies for all atoms.(a) $a = a = 14.1391(3)$ Å, $b = 13.7039(3)$ Å, $c = 13.2935(3)$ Å, $\alpha = \beta = \gamma = 90°$, $\beta = 115.539(2)$ s.g. $P2_1/c$. . $B_{Fe} = 5.4(1)$ Å^2; $B_{Cl} = 4.2(1)$ Å^2; $B_N = 6.7(1)$ Å^2, $B_{C,H} = 7.9(1)$ Å^2.(b) a =

13.9037(6) Å, b = 13.5621(6) Å, c = 13.1303(6) Å, $\alpha = \beta = \gamma = 90º$, β =115.453(3) º s.g. $P2_1/c$. B_{Fe} = 0.8(2) Å^2; B_{Cl} = 0.8(1) Å^2; B_N = 1.5(2) Å^2, , B_C = 1.0(1) Å^2, B_H = 3.4(2) Å^2

Table S6. Estimated parameters from the Mössbauer spectra of Dimim[$FeCl_4$] for phase **I-a** and **I-b** taken at different temperatures.

T (K)	IS (mm/s)	QS (mm/s)	(2ε) (mm/s)	B_{hf} (T)	Γ (mm/s)	I
			Phase I-a			
70	0.34	0.22	-	-	0.37	100
10	0.33	0.22	-	-	0.38	100
4.0	0.33	0.22	-	-	0.37	100
2.1	0.31	0.20	-	-	0.37	100
1.9	0.32	0.22	-	-	0.54	100
			Phase I-b			
70	0.33	0.21	-	-	0.37	100
6	0.34	0.19	-	-	0.36	100
4.0	0.33	-	0.17	27.1	0.31	48
	0.33	-	0.04	28.7	0.31	46
	0.33	0.15	-	-	0.34	6
3.0	0.33	-	0.09	38.1	0.33	48
	0.33	-	0.12	39.0	0.32	46
	0.32	0.15	-	-	0.29	6
2.1	0.33	-	0.07	41.5	0.35	49
	0.32	-	0.15	42.9	0.35	45
	0.33	0.18	-	-	0.33	6
1.9	0.33	-	0.04	42.7	0.37	48
	0.33	-	0.18	44.1	0.36	46
	0.33	0.19	-	-	0.34	6

IS, isomer shift relative to metallic Fe at 295K; QS, quadrupole splitting of doublets; (2ε) quadrupole shift for magnetic sextets; B_{hf} magnetic hyperfine field. Estimated standard deviations are < 0.02 mm/s for IS, QS and (2ε), <0.5T for B_{hf} .

Table S7. Basis vectors of the four possible irreducible representation of the space group $P2_1/c$ for **k** = (0, 0, 0) for the $Fe(1)^{3+}$ and $Fe(2)^{3+}$ ions located on the (0.0930, 0.7410, 0.1500) and (0.4080, 0.2550, 0.0660) positions, respectively.

	x, *y*, *z*	-*x*, *y*+1/2, -*z*+1/2	-*x* ,-*y* ,-*z*	*x* ,-*y*-1/2, *z*-1/2
Γ_1	(100)(010)(001)	(-100)(010)(00-1)	(-100)(0-10)(00-1)	(100)(0-10)(001)
Γ_2	(100)(010)(001)	(-100)(010)(00-1)	(100)(010)(001)	(-100)(010)(00-1)
Γ_3	(100)(010)(001)	(100)(0-10)(001)	(-100)(0-10)(00-1)	(-100)(010)(00-1)
Γ_4	(100)(010)(001)	(100)(0-10)(001)	(100)(010)(001)	(100)(0-10)(001)

Table S8. Final refined positional coordinates from DFT calculations at 0 K for Phase I-b For the phase I-a these are included in Ref 28 of the manuscript.

	Dimim[$FeCl_4$] phaseI-b at 0 K		
Atom	*x/a*	*y/b*	*z/c*
Fe1	0.59348191	0.75665654	0.43810872
Cl1a	0.55016966	0.61475831	0.48225811
Cl2a	0.76309147	0.77793962	0.53832890
Cl3a	0.51008025	0.87654072	0.47537285
Cl4a	0.56306780	0.75906879	0.25952253
N1	0.77000268	0.95249600	0.85514358
C2	0.79392185	0.01112444	0.94157203
N3	0.71301673	0.06824115	0.92232195
C4	0.63551620	0.04538282	0.82105631
C5	0.67111947	0.97293592	0.77904674
C1'	0.83668056	0.87755668	0.84483895
C1"	0.70774281	0.14205202	0.99701624
H2	0.86608427	0.01228633	0.01382393
H4	0.56362619	0.08358960	0.78753623
H5	0.63507541	0.93422950	0.70282098
H1A'	0.82050779	0.86958606	0.75843473
H1B'	0.82172304	0.81095932	0.87710966
H1C'	0.91660722	0.89806816	0.89131502
H1A"	0.67314031	0.20565605	0.94912639
H1B"	0.78535432	0.15762574	0.05775610
H1C"	0.66045179	0.11713041	0.03730834
Fe2	0.08551877	0.73680022	0.14684002
Cl1b	0.03047235	0.61580881	0.21836829
Cl3b	0.01713426	0.87874255	0.15637262
Cl2b	0.25663029	0.74686311	0.23967546
Cl4b	0.04392564	0.70300669	0.96913173
N1b	0.24467341	0.46445719	0.18841636
C2b	0.19526848	0.47965906	0.07972900
N3b	0.25780201	0.52892687	0.04740026
C4b	0.34950986	0.54573146	0.13812216
C5b	0.34134859	0.50519726	0.22628776
C1'b	0.20507078	0.40915879	0.25479915
C1"b	0.23373065	0.55789705	0.93436010
H2b	0.11891994	0.45518494	0.02698389
H4b	0.41111244	0.58571422	0.13215515
H5b	0.39472002	0.50265771	0.31177660
H1A'b	0.12320175	0.39700965	0.20730263
H1B'b	0.21753840	0.44912483	0.32885141
H1C'b	0.24606845	0.34163290	0.27748439
H1A"b	0.15663966	0.53361456	0.88093816
H1B"b	0.29002225	0.52622516	0.90973000
H1C"b	0.23716547	0.63515567	0.93001858

Table S9. Most Relevant Interatomic Distances in the crystal structures of phase I-a at 100 K, phase II at 300 K and phase I-b at 220 K obtained from Rietveld refinements of synchrotron powder diffraction data.

(a)

	Phase I-a 100K		Phase II 300K	
	length (Å)	angle (º)	length (Å)	angle (º)
[FeCl]⁻···[Dimim]⁺ (potential π-d interactions)				
Fe1-Cl1··centroid1	3.936(8)	81.1(2)	-	-
Fe1-Cl3··centroid1	3.901(8)	80.9(2)	3.990(11)	82.1(3)
[Cl]⁻··· [Cl]⁻				
Cl3···Cl4	3.610(6)			
Cl1···Cl2	3.678(6)		3.92(1)	
Cl1···Cl3	3.815(6)		3.92(2)	
Cl1···Cl4			3.97(1)	
Cl2···Cl3			3.94(1)	

(b)

	Phase I-b 220 K	
	length (Å)	angle (º)
[FeCl]⁻···[Dimim]⁺ (potential π-d interactions)		
Fe1-Cl1··centroid1	3.76(1)	90.5(4)
Fe2-Cl2b··centroid1	3.55(2)	96.1(4)
Fe2-Cl2b··centroid2	3.77(1)	88.4(4)
Fe1-Cl4··centroid2	3.72(1)	85.6(4)
[Cl]⁻··· [Cl]⁻		
Cl1···Cl1	3.48(2)	
Cl4···Cl1b	3.82(1)	
Cl3···Cl3	3.80(2)	
Cl1b···Cl3b	3.76(1)	
Cl4···Cl3b	3.95(1)	
Cl2···Cl3	3.94(1)	
Cl2b···Cl3	3.95(1)	

References:

[1]. J. Stewart; P. Deen, K. Andersen, H. Schober, J.F. Barthélémy, J. Hillier, A. Murani, T. Hayes, B. Lindenau *Journal of Applied Crystallography* **2009**, *42*, 69-84.
[2]. O. Schärpf, H. Capellmann *physica status solidi (a)* **1993**, *135*, 359-379.
[3]. J. M. Soler, E. Artacho, J. D. Gale, A. García, J. Junquera, P. Ordejón and D. Sánchez Portal, *Journal of Physics: Condensed Matter* **2002**, 14, 2745-2779.
[4]. G. Román-Pérez and J. M. Soler, *Physical review letters* **2009**, 103, 096102.
[5]. M. Dion, H. Rydberg, E. Schröder, D. C. Langreth and B. I. Lundqvist *Physical review letters* **2004**, 92, 246401.
[6]. J. Kohanoff, C. Pinilla, T. G. Youngs, E. Artacho and J. M. Soler *The Journal of chemical physics,*, **2011**, 135, 154505.
[7]. N. Troullier and J. L. Martins *Physical review B,* **1991**, 43, 1993-2006.
[8]. L. Kleinman and D. M. Bylander *Physical Review Letters,* **1982**, 48, 1425-1428.
[9]. S. G. Louie, S. Froyen and M. L. Cohen *Physical Review B,* **1982**, 26, 1738-1742.
[10]. E. Artacho, D. Sánchez-Portal, P. Ordejón, A. García and J. M. Soler *Phys. Status Solidi B*, **1999**, 215, 809-817.
[11]. H. J. Monkhorst and J. D. Pack *Physical Review B* **1976**, 13, 5188-5192.
[12]. J. Moreno and J. M. Soler *Physical review B* **1992**, 45, 13891-13898.
[13]. M. Leslie and N. Gillan *Journal of Physics C: Solid State Physics,***1985**, 18, 973.
[14] A. Boultif, D. Louer *Journal of Applied Crystallography* **2004**, *37*, 724.

[15] O. Vallcorba, J. Rius, C. Frontera, I. Peral, C. Miravitlles, *Journal of Applied Crystallography* **2012**, *45*, 844-848.
[16] O. Vallcorba, J. Rius, C. Frontera, C. Miravitlles, *Journal of Applied Crystallography* **2012**, *45*, 1270-1277.
[17] J. Rius, *RIBOLS18: A computer program for least-squares refinement from powder diffraction data; Institut de Ciencia de Materialsde Barcelona [CSIC]*, Barcelona, Spain, **2009**.
[18] I.J. Bruno, J.C. Cole, M. Kessler, J. Luo, W.D. Motherwell, L. H. Purkis, B.R. Smith, R. Taylor, R. I. Cooper, S.E. Harris, A.G. Orpen, *Journal of Chemical Information and Computer Sciences* **2004**, *44*, 2133-2144.
[19] I. de Pedro, J.M. Rojo, J. Luis Pizarro, J. Rodriguez Fernandez, J. Sanchez Marcos, M. Teresa Fernandez-Diaz, M.I. Arriortua, T. Rojo *Journal of Materials Chemistry* **2007**, *17*, 3915-3923.
[20] I. de Pedro, J.M. Rojo, V. Jubera, J. R. Fernandez, J.S. Marcos, L. Lezama, T. Rojo *Journal of Materials Chemistry* **2004**, *14*, 1157-1163.
[21] E. Bertaut *Acta Crystallographica Section A: Crystal Physics, Diffraction, Theoretical and General Crystallography,* **1968**, *24*, 217-231.
[22] E. Arunan, G. R. Desiraju, R. A. Klein, J. Sadlej, S. Scheiner, I. Alkorta, D. C. Clary, R. H. Crabtree, J. J. Dannenberg, P. Hobza, H. G. Kjaergaard, A. C. Legon, B. Mennucci, D. J. Nesbitt *Pure and Applied Chemistry* **2011**, *83*, 1637-1641.
[23] Y. S. Rosokha, S. V. Lindeman, S. V.; Rosokha, J. K. Kochi, *Angewandte Chemie International Edition,* **2004**, *43*, 4650-4652.